IEEE Photonics Journal
An IEEE Photonics Society Publication

Open Access

Monolithic Integrated Silicon Photonic Interconnect With Perfectly Vertical Coupling Optical Interface

Volume 5, Number 5, October 2013

Zanyun Zhang
Beiju Huang
Zan Zhang
Chuantong Cheng
Hongda Chen, Member, IEEE

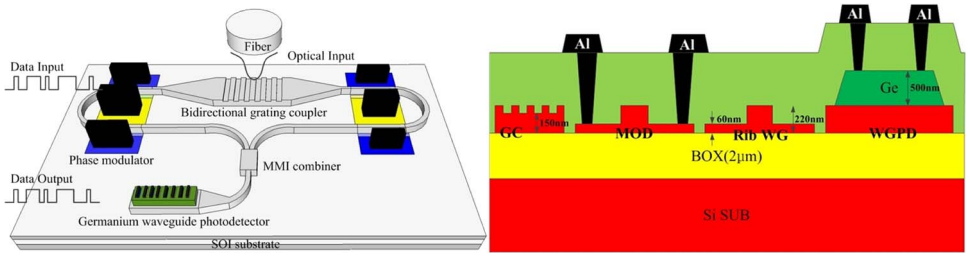

DOI: 10.1109/JPHOT.2013.2281978
1943-0655

Monolithic Integrated Silicon Photonic Interconnect With Perfectly Vertical Coupling Optical Interface

Zanyun Zhang, Beiju Huang, Zan Zhang, Chuantong Cheng, and Hongda Chen, *Member, IEEE*

State Key Laboratory on Integrated Optoelectronics, Institute of Semiconductors, Chinese Academy of Sciences, Beijing 100083, China

DOI: 10.1109/JPHOT.2013.2281978

Manuscript received August 15, 2013; revised September 3, 2013; accepted September 5, 2013. Date of publication September 16, 2013; date of current version September 24, 2013. This work was supported in part by the National Basic Research Program of China under Grants 2011CBA 00608, 2010CB934104, and 2011CB933203; by the National Natural Science Foundation of China under Grants 61036002, 61178051, 61021003, 61036009, 61076023, and 61178081; and by the National High Technology Research and Development Program ("863"Program) of China under Grants 2013AA013602, 2013AA031903, and 2012AA030608. Corresponding author: B. Huang (e-mail: bjhuang@semi.ac.cn).

Abstract: We proposed and demonstrated a point-to-point photonic interconnect based on a perfectly vertical grating coupler. This bidirectional grating plays double roles of coupling and splitting at the optical input. Based on such a configuration, an electro-optical (E-O) modulator and photonic interconnect were demonstrated. To characterize the photonic interconnect, both the E-O modulator and germanium waveguide photodetector were measured. Finally, an eye diagram test was carried out to study the dynamic performance of the photonic link. The results show that the maximum operation speed is 4 Gb/s.

Index Terms: Silicon nanophotonics, perfectly vertical coupling, waveguide grating coupler, waveguide devices, silicon photonic interconnect.

1. Introduction

Optical interconnects with silicon photonics have been attracting more and more attention because of its complementary metal-oxide-semiconductor (CMOS) compatibility and various advantages compared with electrical interconnects such as low latency, high bandwidth, low power consumption and low mutual interference [1]. By processing alongside existing mature CMOS technology, the manufacturing cost of photonics devices will be reduced greatly and the integration level will be increased drastically.

In the past few years, numerous impressive works have been reported in silicon photonics, especially in the study of critical devices such as light sources [2]–[5], fiber couplers [6]–[8], WDM passive devices [9], [10], optical modulators [11]–[13] and Germanium waveguide photodetectors [14]–[16]. To develop a full on-chip optical interconnect, a point-to-point photonic interconnect with on-chip light source, optical modulator and germanium waveguide photodetector is considered to be the basic practice of integration. However, because present hybrid lasers [3]–[5] are highly process demanding, only a few works [17], [18] have demonstrated photonic interconnect with integrated light source so far. Furthermore, the high cost and low yielding of such hybrid light sources also hinder them from large-scale integration and application. Therefore, fiber couplers, which function as on-chip optical interfaces with external light source, are still of paramount

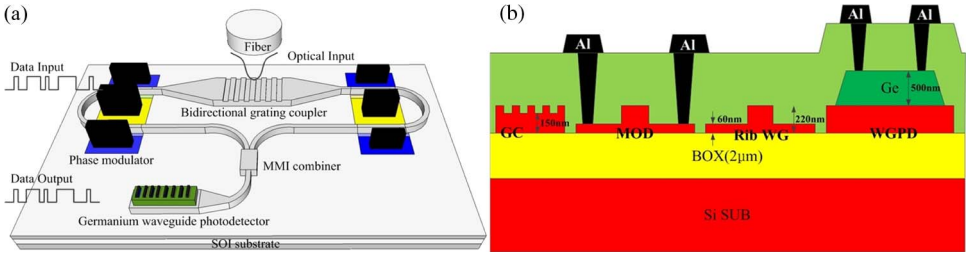

Fig. 1. (a) Schematic layout of the integrated photonic interconnect. (b) Cross-section diagrams of the photonic components.

importance. As a proof-of-concept, several works [19]–[21] have been reported on the integration of fiber coupler, optical modulator and germanium waveguide photodetector. Among these works, Nano-taper spot-size converter [6], [7] and grating coupler are the most popular fiber couplers. Nano-taper coupler is both compact and low-loss, but suffers from its submicron misalignment tolerance and costly edge polishing process. Grating coupler has many advantages such as large alignment tolerance, wafer-scale testability and placement flexibility. Unfortunately, in order to avoid large second order reflection, grating couplers in photonic integrated circuits [22], [23] are mostly designed for tilted fiber coupling. This will bring two main disadvantages. Firstly, fiber angle tuning in wafer-scale test will be quite time consuming. Secondly, unavoidable angle polishing [24], [25] in fiber packaging will lead to additional cost. Therefore, an optimal fiber coupler for rapid wafer-scale test and low-cost packaging will be a demand for on-chip optical interconnects.

In our prior work, we demonstrated a perfectly vertical grating coupler with quasi Mach-Zehnder characteristics on silicon-on-insulator (SOI) substrate [26]. In this paper, we proposed and demonstrated a monolithic integrated photonic interconnect based on such configuration. To the best of our knowledge, such an integration method has never been reported before. This basic photonic interconnect presented here can serve as a low-cost building block for developing scalable optical interconnection architectures in the next generation on-chip optical networks.

2. Overview of the Photonic Interconnect

2.1. Configuration and Principle

The photonic interconnect is a point-to-point on-chip photonic link integrated with bidirectional grating coupler, optical phase modulator, multimode interferometer (MMI) optical combiner and germanium waveguide photodetector (WGPD). Fig. 1(a) and (b) shows the schematic layout and cross-section diagrams of the photonic interconnect respectively. In this configuration, the bidirectional grating plays double roles of both vertical fiber coupler and 3-dB optical splitter at the optical input. The light beam launched from a perfectly vertical fiber is coupled in and split in to two parts with opposite directions by the bidirectional grating. Due to the symmetry of the bidirectional uniform grating, the power splitting ratio will be a perfect 50:50 with the fiber perfectly aligned at the grating center. In order to transmit light in low loss and realize phase modulating, each side of the grating is transformed to a single mode rib waveguide arm using linear taper waveguide. Then by embedding a carrier depletion type phase shifter in both arms, the optical phase of two waves can be changed individually or simultaneously. To combine the optical power in two arms, a 1×2 MMI coupler is used as the optical combiner. At the same time, optical phase modulation of the two arms is converted to intensity modulation at the MMI output end. When a $\eth$ phase shift is introduced between the light in two arms, a strong destructive interference will occur and thus modulate the optical signal to low level. Therefore, a proper driving external signal can drive the modulator "on" and "off" and thus imprinting the electrical data input onto the optical signal. Then the modulated optical signal is transmitted to the detector block and converted back to the electrical data.

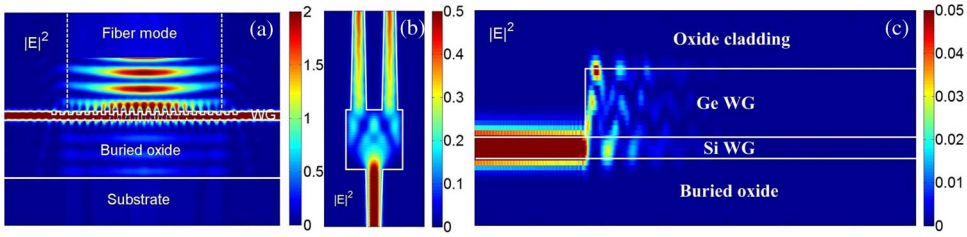

Fig. 2. Simulated electric field intensity distribution of (a) the grating cross-section, (b) the MMI combiner, and (c) the waveguide photodetector cross-section.

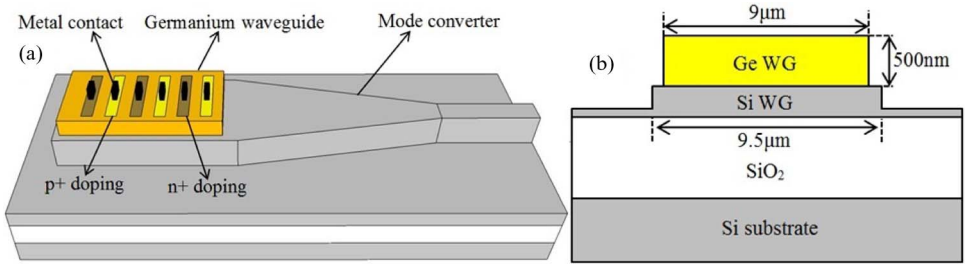

Fig. 3. (a) Schematic layout of the germanium waveguide photodetector. (b) Cross-sectional view of the detector waveguide configuration.

2.2. Design and Fabrication

The photonic interconnect is designed and realized in a 220-nm-thick silicon waveguide layer on a 2-μm-thick buried oxide. The optical components were carefully designed and their functions were simulated and verified by 3-D finite difference time domain (FDTD) method. As a key component, the bidirectional grating is designed to be a uniform grating coupler for perfectly vertical coupling with optimal geometrical parameters of 580 nm grating period, 70 nm etch depth, filling factor of 47%, and 22 periods [26]. The final design are verified by 3-D FDTD simulation, in which a Gaussian source with 1/e full width of 10.4 μm was employed to represent the fiber launch mode and the background index was set to be 1.46 so as to simulate the effect of the oxide cladding layer. Fig. 2(a) shows the simulated electric field intensity distribution of the grating cross-sectional view. Functions of both coupling and splitting can be clearly observed. Followed by an adiabatic linear taper of 200 μm at each side, the bidirectional grating is connected to two single mode waveguide arms which are 500 nm wide ridge waveguides with a slab thickness of 60 nm.

Fig. 2(b) shows the electric field intensity distribution of the MMI coupler, which functions as an optical combiner. In order to enhance the coupling efficiency, this 1 $\times$ 2 MMI is designed to have a tapered waveguide at both input and output, which is similar to the design in [27]. The tapered waveguide ports are widened to a width of 1 μm from the uniform waveguide width of 500 nm. In order to minimize the transmission loss, the linear taper length is designed to be 10 μm. The width of the MMI region is chosen as 3 μm. According to the self-imaging theory and our simulation results, the length of the MMI region and the separation between the two waveguides are designed to be 8.2 μm and 1.6 μm respectively. The designed insertion loss is at a low value of 0.75 dB.

As shown in Fig. 3(a), the WGPD in this photonic link is designed to be an evanescently coupled photodetector with interleaved lateral p-i-n configurations. The germanium waveguide layer is 500 nm thick and with an footprint of 9 $\times$ 25 μm^2. To reduce the reflection at the detector interface, a silicon taper waveguide of 40 μm is utilized. Assuming the absorption coefficient of strained germanium as 4000 cm^{-1} [28], we simulated the light absorption with a detector length of 25 μm, the cross-sectional view of which is shown in Fig. 2(c). The simulation results indicate this would be enough for fully absorption and detection. For the p-i-n diode, the p+/n+ doping concentration is about 10^{19} cm^{-3}, and the i-Ge width is designed as 1.5 μm.

Fig. 4. (a) Top-view of the phase modulator design. (b) Cross-sectional view of the phase modulator design.

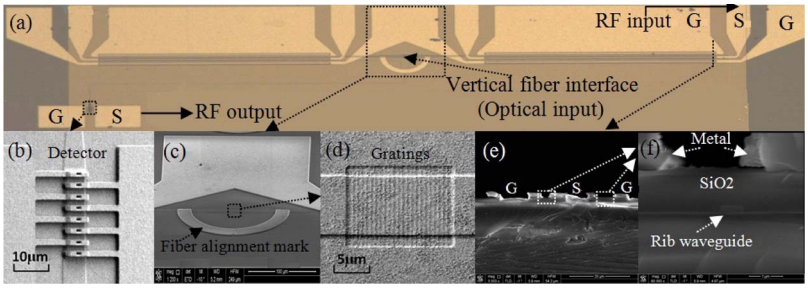

Fig. 5. (a) Microscope photo of the integrated photonic interconnect. (b) SEM top images of the integrated germanium waveguide photodetector. (c) Top view of the optical interface. (d) The gratings with silicon dioxide cladding layer. (e) The cross-sectional view of the phase shifter with GSG electrode pattern. (f) Zoomed cross-sectional view of the rib waveguide embedded in the phase shifter.

In order to realize optical modulation function, two carrier-depletion type phase shifters are embedded in the two waveguide arms respectively. Furthermore, an arm length difference of 30 μm is introduced to make the modulation wavelength dependent. Fig. 4 shows the phase modulator design. To make the device more compact, we designed a symmetrical phase shifter in which two PN junctions are parallel. The two parallel PN junctions are embedded in the upper and lower waveguide of one folded waveguide arm respectively. The phase modulator is 800 μm long while gives an effective phase modulation length of 1.6 mm. The P-type doping concentration is 7×10^{17} cm^{-3}, and the N-type doping concentration is about 5×10^{17} cm^{-3}. In order to increase the overlap between holes and optical mode, the P doped region in the waveguide ridge is designed to be 350 nm wide. To isolate the optical mode from the heavy loss contact regions, the P++ and N++ regions with doping concentration of 10^{20} cm^{-3} are located 1 μm away from the ridge side.

The entire chip is fabricated on a 200 mm in diameter SOI wafer, using standard CMOS compatible technology. Fig. 5 shows the microscope photo of the integrated photonic link and the SEM images of various components. As shown in Fig. 5(c), a metal ring alignment mark with an inner diameter of 125 μm was designed and fabricated to help the fiber alignment. The simplified process integration flow of the photonic link is as follows. The rib waveguides (etch depth of 160 nm) and gratings (etch depth of 70 nm) were formed sequentially using 193 nm deep UV lithography and anisotropic dry etching, after which the p++, p, n, n++ implants for modulators were performed with different dose and energy. The implanted dopants in silicon were activated using a rapid thermal anneal (RTA) at 1030° for 5 s prior to Ge epitaxy. Then, a 60 nm SiO_2 layer was deposited and etched to form a window, at which Ge was selectively grown to a thickness of 500 nm using ultrahigh vacuum chemical vapor deposition (UHVCVD). Then, in order to eliminate the lattice mismatch and defects for performance enhancement, the samples further underwent a postepitaxy annealing step at 750° for 30 min. Ion implantation was then performed for the p+ and n+ doping of the lateral Ge photodetector. These dopants in Ge were also activated by annealing at 500° for 5 min. After 1.1 μm SiO_2 cladding layer was deposited, contacts and aluminum interconnects were

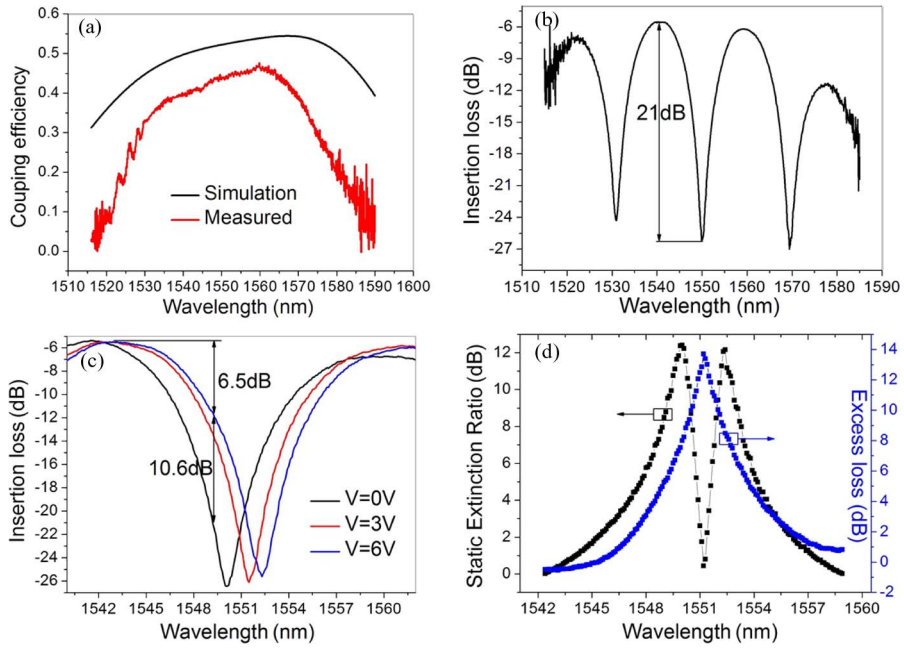

Fig. 6. (a) Comparison between the simulated and measured coupling efficiency of the bidirectional grating. (b) Comparison between the normalized grating coupling curve and modulator transmission. (c) Modulator spectral response with different driving voltage. (d) Wavelength dependent relationship of the static ER and IL.

formed and patterned as the last step. The fiber alignment mark is also fabricated using the aluminum electrode layer.

3. Experimental Work

3.1. Characterization of Optical Modulator

The E-O modulator here we are discussing is comprised by the bidirectional grating coupler, MMI combiner and phase modulators. As grating is part of the modulator, the grating behavior is very important to the modulator. By measuring a bidirectional grating with balanced arms, we obtained the coupling efficiency of the coupler (the total coupling efficiency of the two directions). The comparison between the simulated and measured coupling curve is depicted in Fig. 6(a). We can see that they coincides well in curve trend with a flat-top filtering characteristics. Compared with the simulated efficiency of 53%, the measured result is a bit lower with a peak coupling efficiency of 46%. According to our simulation, this calculated coupling efficiency can even be increased to 66% by introducing a bottom metal mirror using CMOS compatible postprocessing. The normalized optical transmission of the modulator is depicted in Fig. 6(b). Because its unbalanced arms, strong optical interference pattern was obtained as expected. The total insertion loss (IL) of the modulator is about 5.5 dB, which includes 3.3 dB coupling loss, 1.1 dB MMI coupler loss and 1.1 dB phase shifter doping loss. The notch depth of the interference pattern exceeds 20 dB, which indicates the grating functions well as the 3-dB splitter. Fig. 6(c) shows the spectral response of the modulator under different driving voltages. The spectrum shifts are 1.6 nm and 2.5 nm with bias voltage of 3 V and 6 V respectively, giving a modulation efficiency of 2.88 V · cm and 3.68 V · cm. Fig. 6(d) shows the wavelength dependent relationship of the modulator static extinction ratio (ER) and IL. In order to obtain a high extinction ratio while not introducing too much excess loss, the working wavelength of 1549 nm is chosen for eye diagram test. The excess loss and the static extinction ratio at 1549 nm are 6.5 dB and 10.6 dB, respectively, with reverse bias of 6 V.

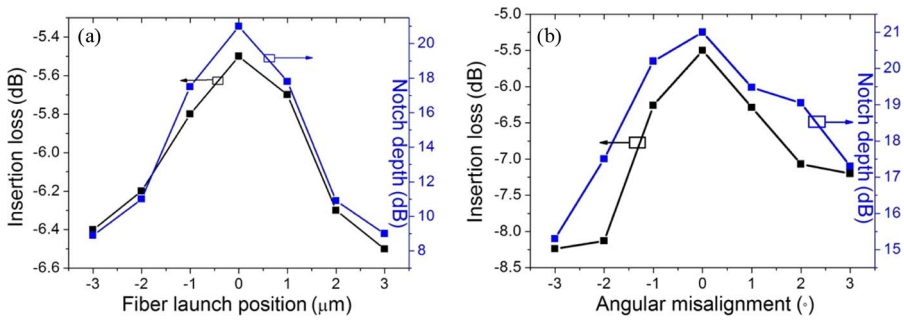

Fig. 7. Misalignment tolerance of the modulator insertion loss and notch depth on (a) fiber launch position and (b) fiber launch angle.

The device performance in Fig. 6(a) is obtained when the fiber is nearly perfectly aligned at the grating region (perfectly vertical right in the grating center). In order to investigate the fiber misalignment tolerance of the modulator, we measured the insertion loss and the notch depth of the modulator transmission spectrum at different fiber positions and different launch angles by carefully tuning the fiber in both lateral direction and the angular plane. Here, we define the maximum transmission point as the modulator IL and the maximum static ER as the notch depth. Fig. 7(a) shows the insertion loss and notch depth variation within ± 3 μm fiber tuning range. The excess loss within 1 dB shows the modulator insertion loss is quite misalignment tolerant to fiber position change. Compared to the insertion loss, the notch depth is more sensitive to the fiber position change. However, within the ± 1 μm range, the notch depth decrease is no more than 4 dB. This should be enough for the modulator application. In the angular misalignment measurement, the measured transmission spectra at different fiber angles were not obtained with the same fiber launch position. This is because when the fiber angle is changed relative to vertical, the fiber lateral position changes too. Therefore, after fixing the fiber launch angle, the fiber position was carefully tuned to find the spectrum with the largest interference pattern. Generally, with the fiber angle varying, the best fiber position for a modulator will also change to balance the splitting ratio of the two arms. Fig. 7(b) shows the angular misalignment tolerance of the modulator IL and notch depth. We can see that the IL increase is no more than 3 dB within the $\pm 3^{\circ}$ angle range off vertical. For the notch depth, the minimum value at -3° exceeds 15 dB. This tells that the device will still be effective even with a small fiber angle misalignment.

The data transmission experiment was carried out to demonstrate the dynamic operation capability of such a modulator. A signal quality analyzer (Anritsu MP1800A) was used to provide a high speed pseudorandom binary sequence (PRBS) data stream with a pattern length of $2^{31} - 1$. After amplification using a microwave amplifier, the driven signal with peak to peak value of 6 V and 3 V reverse bias was fed to the modulator through a microwave probe. The optical output was directly coupled to a digital communication analyzer (Agilent DCA 86100C) with a 12 GHz optical head. Fig. 8(a) and (b) show the optical eye diagrams at a data rate of 10 Gb/s and 12.5 Gb/s respectively. Here our device was not terminated under test, because we found that terminating the device was not helpful to either the speed or the extinction ratio. A possible reason is that the symmetrical phase shifter we utilize makes the traveling wave electrode ineffective.

3.2. Characterization of the WGPD

We measured the *I–V* curve of the WGPD within the voltage range of -3 V to 1 V, as shown in Fig. 9(a). The measured dark currents at -1 V and -3 V are 254 nA and 1.35 μA respectively. Considering the active area of the device, the corresponding dark current densities were calculated to be 113 mA/cm^2 and 601 mA/cm^2 respectively. Such a high dark current density can be mainly attributed to the high defect germanium bulk layer caused by the heavy doping of the lateral p-i-n junction.

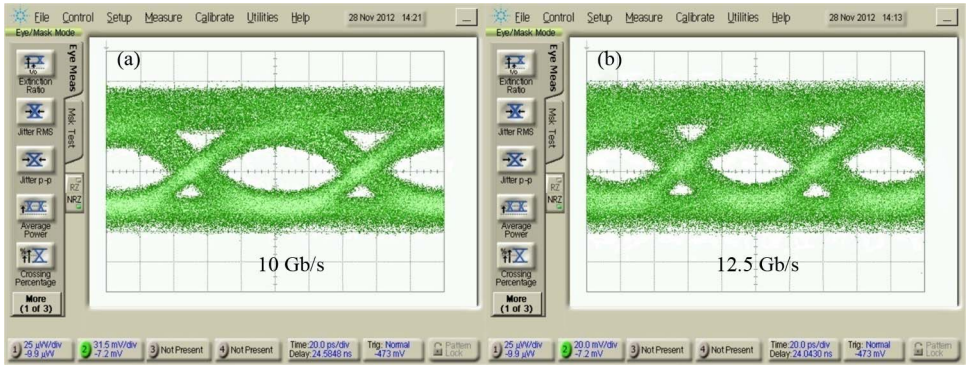

Fig. 8. Eye diagrams of the modulator at data rate of (a) 10 Gb/s and (b) 12.5 Gb/s, respectively.

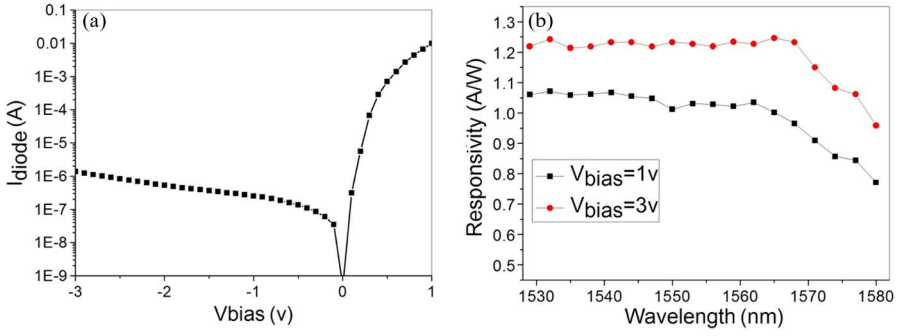

Fig. 9. Characteristics of the WGPD (a) *I*–*V* curve of the WGPD. (b) Responsivity of the WGPD under different reverse bias voltages.

In order to obtain the characteristics of the WGPD, a single detector with the same geometry parameters connected with a nano-taper tip coupler was measured. A lensed fiber with spot size of 2.5 μm was used to interface with the coupler and couple light into the waveguide. The insertion loss of the coupler and waveguide were measured by the neighboring waveguide without the Ge detector. Therefore, we can calculate the responsivity by measuring the photocurrent with the reaching power at the detector input. Fig. 9(b) shows the measured responsivity over the wavelength range from 1528–1580 nm with reverse bias of 1 V and 3 V respectively. A flat responsivity was obtained for the wavelength range out to 1560–1570 nm, which corresponds to the absorption edge of bulk Ge due to the tensile-strain induced bandgap narrowing [28]. The mean values of the flat responsivity range at -1 V and -3 V bias reach as high as 1.06 A/W and 1.21 A/W respectively, corresponding to quantum efficiencies of 85% and 97%. Such high responsivity of the device implies a fully optical absorption in the Germanium active layer.

In order to characterize the dynamic performance of the WGPD, a commercially available $LiNbO_3$ modulator with 12 GHz bandwidth was utilized to test the device. Fig. 10 shows the eye diagrams at a bit rate of 5 Gb/s and 6 Gb/s. It is implied the bandwidth of the WGPD is far below the intrinsic bandwidth of several tens of GHz which is mainly limited by the slow diffusion current from the n and p layers [29]. Using the electron and hole drift saturation velocities of 6×10^6 cm/s, the transit time limited bandwidth for the 1.5-μm-spacing detector is 17.7 GHz. Obviously, the parasitic RC delay dominants the dynamic performance of the device, which is mainly attributed to the large parasitic capacitance from the large probe pad. For our device, the footprint of probe pad is about 150×90 μm^2. According to the results in [30], the pad capacitance can be estimated to be 280 fF. Assuming the pad capacitance is proportional to the area and considering the similar process condition and device geometry, this estimation is reasonable. Comparing with this large parasitic capacitance, the intrinsic depletion capacitance ($\sim$1 fF) is negligible. Assuming the load resistance

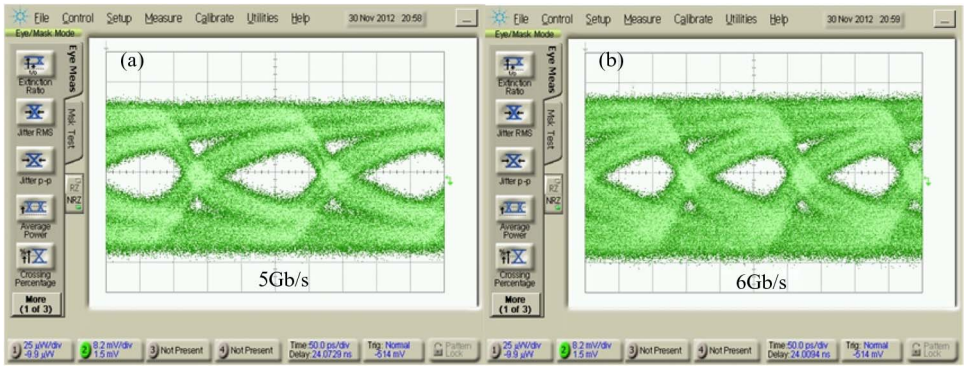

Fig. 10. Eye diagrams of the Germanium WGPD. (a) At 5 Gb/s, (b) At 6 Gb/s.

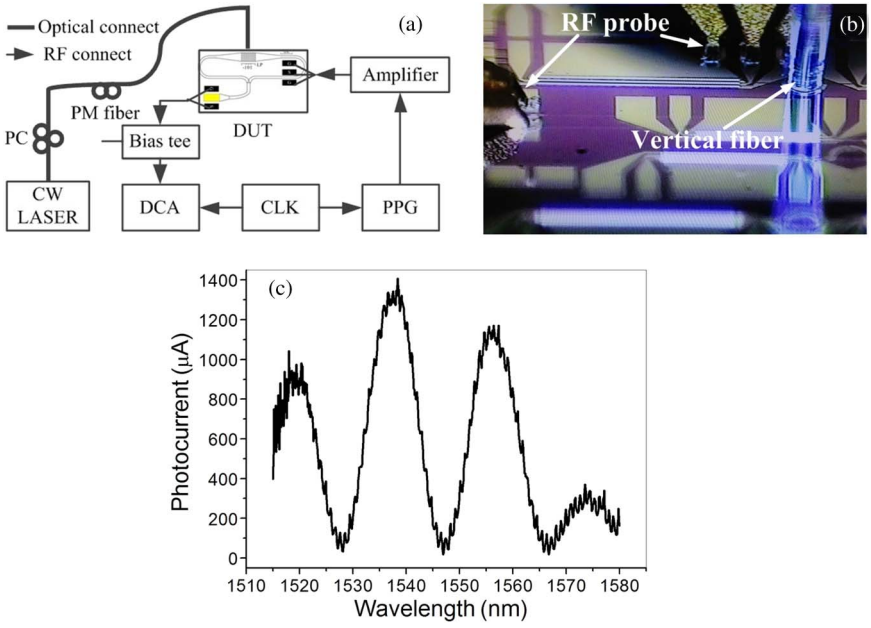

Fig. 11. (a) Experimental setup of the photonic link. (b) Microphotograph of chip under test. (c) DC transmission spectrum of detector response with 1 V detector bias.

as 50 Ω, the RC limited bandwidth is calculated to be 11.3 GHz. Combining these two factors, the estimated overall bandwidth is only 9.53 GHz. Although such a device bandwidth is low, it still overestimates the device's dynamic performance. There may be two possible reasons. Firstly, the load resistance combining the effect of diode series resistance and the interleaved metal line resistance may be underestimated in the assumption. Secondly, the narrow metal interconnection lines may introduce an inductance element. Combining with other elements, this inductance will possibly form a parasitic low-pass-filter that limits the device's speed further. In our future work, the detector bandwidth is expected to be greatly enhanced by decreasing the i-Ge thickness and the probe pad footprint.

3.3. Characterization of the Photonic Interconnect

Fig. 11(a) shows the data transmission experimental setup of the photonic interconnect. Monochromatic light from a CW tunable laser was coupled to a single mode fiber. After polarization controlling (PC), the light was directly coupled to the chip vertically by a polarization maintained

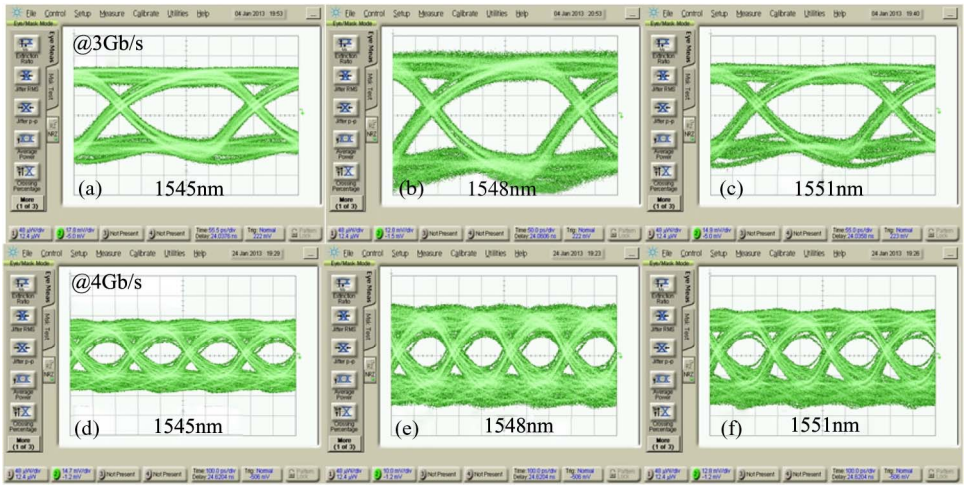

Fig. 12. Eye diagrams at different operation wavelengths with data rate of 3 Gb/s and 4 Gb/s.

(PM) fiber. Because of the low insertion loss of the modulator, optical amplification is no longer necessary. The RF connect is shown with black arrow. The data stream from a PPG (Anritsu MP1800A) was amplified and biased to a modulator driven signal with a voltage swing of 6 V and reverse bias of 3 V. The modulator wasn't terminated in the test just as shown in Fig. 11(b). Detector response was obtained through a RF probe with a GS pattern. With a bias of -1 V, the DC spectrum of the detector response is shown in Fig. 11(c). Due to the grating filtering characteristic and the detecting limit of germanium, the photocurrent response spectrum is not flat and falls off at longer wavelengths. The dip wavelengths are 1528 nm, 1547.6 nm and 1566.5 nm respectively, where destructive interference happens. Also, we can see that the detector response spectrum is not so smooth and shows small ripples. This is possibly attributed to the Fabry-Perot resonance effect caused by the reflection at the grating interface and detector input.

Eye diagrams were recorded by sending non-return-to-zero (NRZ) pseudorandom binary sequence (PRBS) to the modulator through a high speed GSG probe with data rate of 3 Gb/s and 4 Gb/s. The peak-to-peak voltage, pattern length, and bias voltage of the PRBS source signal are 6 V_{pp}, $2^{15} - 1$ and -3 V, respectively. At the detector block, the photocurrent at -1 V bias was directly coupled to a sampling oscilloscope (Agilent DCA 86100C) without any amplification. Fig. 12 shows the eye diagrams obtained at different working wavelengths of 1545 nm, 1548 nm and 1551 nm respectively. This implies this photonic link has a broad working wavelength range. Clear open eyes at 3 Gb/s and 4 Gb/s indicate this photonic link is expected to achieve error free operation under such data rates.

4. Conclusion

To summarize, we proposed and demonstrated a monolithic integrated photonic interconnect based on a perfectly vertical grating coupler. As both the input fiber coupler and 3-dB splitter, the bidirectional grating integrates the grating coupler and optical modulator as a single device. Comprised by a bidirectional grating based E-O modulator and a WGPD, this photonic interconnect can transmit the electrical data in the form of light and then convert it back to the electrical domain. To characterize the photonic interconnect, both the E-O modulator and germanium WGPD were measured and characterized individually. To investigate the dynamic behavior, large signal data transmission experiment were carried out. Clear eye diagrams at 3 Gb/s and 4 Gb/s were obtained. Although such a performance is inferior to the state-of-art, the bandwidth of this photonic interconnect can be increased drastically by utilizing the travelling wave modulator and optimizing the WGPD. Such a point-to-point photonic link can be further extended to on-chip wavelength-division multiplexing (WDM) system by introducing the MUX/DEMUX functions.

References

[1] D. A. B. Miller, "Rationale and challenges for optical interconnects to electronic chips," *Proc. IEEE*, vol. 88, no. 6, pp. 728–749, Jun. 2000.

[2] N. Fujioka, T. Chu, and M. Ishizaka, "Compact and low power consumption hybrid integrated wavelength tunable laser module using silicon waveguide resonators," *IEEE J. Lightw. Technol.*, vol. 28, no. 21, pp. 3115–3120, Nov. 2010.

[3] A. W. Fang, H. Park, O. Cohen, R. Jones, M. J. Paniccia, and J. E. Bowers, "Electrically pumped hybrid AlGaInAs-silicon evanescent laser," *Opt. Exp.*, vol. 14, no. 20, pp. 9203–9210, Oct. 2006.

[4] S. Tanaka, S. Jeong, S. Sekiguchi, T. Kurahashi, Y. Tanaka, and K. Morito, "High-output-power, single-wavelength silicon hybrid laser using precise flip-chip bonding technology," *Opt. Exp.*, vol. 20, no. 27, pp. 28057–28069, Dec. 2012.

[5] S. Messaoudene, S. Keyvaninia, C. Jany, F. Poingt, F. Lelarge, G. De Valicourt, G. Roelkens, D. Van Thourhout, F. Lelarge, J. Fedeli, and G. Duan, "Low-threshold heterogeneously integrated InP/SOI lasers with a double adiabatic taper coupler," *IEEE Photon. Technol. Lett.*, vol. 24, no. 1, pp. 76–78, Jan. 2012.

[6] D. Vermeulen, S. Selvaraja, P. Verheyen, G. Lepage, W. Bogaerts, P. Absil, D. Van Thourhout, and G. Roelkens, "High-efficiency fiber-to-chip grating couplers realized using an advanced CMOS-compatible silicon-on-insulator platform," *Opt. Exp.*, vol. 18, no. 17, pp. 18278–18283, Aug. 2010.

[7] C. Kopp, S. Bernabe, B. B. Bakir, J. Fedeli, R. Orobtchouk, F. Schrank, H. Porte, L. Zimmermann, and T. Tekin, "Silicon photonic circuits: On-CMOS integration, fiber optical coupling, and packaging," *IEEE J. Sel. Top. Quantum. Electron.*, vol. 17, no. 3, pp. 498–509, May/Jun. 2011.

[8] M. Pu, L. Liu, H. Ou, K. Yvind, and J. M. Hvam, "Ultra-low-loss inverted taper coupler for silicon-on-insulator ridge waveguide," *Opt. Commun.*, vol. 283, no. 19, pp. 3678–3682, Oct. 2010.

[9] Q. Fang, Y. T. Phang, C. W. Tan, T. Liow, M. B. Yu, G. Q. Lo, and D. L. Kwong, "Multi-channel silicon photonic receiver based on ring-resonators," *Opt. Exp.*, vol. 18, no. 13, pp. 13510–13515, Jun. 2010.

[10] F. Horst, "Silicon integrated waveguide devices for filtering and wavelength demultiplexing," in *Proc. Conf. OFC, collocated Nat. Fiber Optic Eng. Conf.*, 2010, pp. 1–3.

[11] F. Y. Gardes, D. J. Thomson, N. G. Emerson, and G. T. Reed, "40 Gb/s silicon photonics modulator for TE and TM polarisations," *Opt. Exp.*, vol. 19, no. 12, pp. 11804–11814, Jun. 2011.

[12] T. G. Neogi, S. Deng, J. Novak, J.-R. Guo, R. Clarke, M. R. LeRoy, J. F. McDonald, and Z. R. Huang, "Modeling and analysis of an 80-Gbit/s SiGe HBT electrooptic modulator," *IEEE Photon. J.*, vol. 3, no. 1, pp. 42–56, Feb. 2011.

[13] S. Deng, T. G. Neogi, J. Novak, J. McDonald, and R. Huang, "Design of short electro-optic modulator based on SiGe HBT structure," *Opt. Exp.*, vol. 18, no. 3, pp. 1994–2001, Feb. 2010.

[14] S. Liao, N. Feng, D. Feng, P. Dong, R. Shafiiha, C. Kung, H. Liang, W. Qian, Y. Liu, J. Fong, J. E. Cunningham, Y. Luo, and M. Asghari, "36 GHz submicron silicon waveguide germanium photodetector," *Opt. Exp.*, vol. 19, no. 11, pp. 10967–10972, May 2011.

[15] T. Yin, R. Cohen, M. M. Morse, G. Sarid, Y. Chetrit, D. Rubin, and M. J. Paniccia, "31 GHz Ge n-i-p waveguide photodetectors on silicon-on-insulator substrate," *Opt. Exp.*, vol. 15, no. 21, pp. 13965–13971, Oct. 2007.

[16] C. T. DeRose, D. C. Trotter, W. A. Zortman, A. L. Starbuck, M. Fisher, M. R. Watts, and P. S. Davids, "Ultra compact 45 GHz CMOS compatible germanium waveguide photodiode with low dark current," *Opt. Exp.*, vol. 19, no. 25, pp. 24897–24904, Dec. 2011.

[17] Y. Urino, T. Shimizu, M. Okano, N. Hatori, M. Ishizaka, T. Yamamoto, T. Baba, T. Akagawa, S. Akiyama, T. Usuki, D. Okamoto, M. Miura, M. Noguchi, J. Fujikata, D. Shimura, H. Okayama, T. Tsuchizawa, T. Watanabe, K. Yamada, S. Itabashi, E. Saito, T. Nakamura, and Y. Arakawa, "First demonstration of high density optical interconnects integrated with lasers, optical modulators, and photodetectors on single silicon substrate," *Opt. Exp.*, vol. 19, no. 26, pp. B159–B165, Dec. 2011.

[18] Y. Urino, Y. Noguchi, M. Noguchi, M. Imai, M. Yamagishi, S. Saitou, N. Hirayama, M. Takahashi, H. Takahashi, E. Saito, M. Okano, T. Shimizu, N. Hatori, M. Ishizaka, T. Yamamoto, T. Baba, T. Akagawa, S. Akiyama, T. Usuki, D. Okamoto, M. Miura, J. Fujikata, D. Shimura, H. Okayama, H. Yaegashi, T. Tsuchizawa, K. Yamada, M. Mori, T. Horikawa, T. Nakamura, and Y. Arakawa, "Demonstration of 12.5-Gbps optical interconnects integrated with lasers, optical splitters, optical modulators and photodetectors on a single silicon substrate," *Opt. Exp.*, vol. 20, no. 26, pp. B256–B263, Dec. 2012.

[19] G. Roelkens, D. Vermeulen, S. Selvaraja, R. Halir, W. Bogaerts, and D. Van Thourhout, "Grating-based optical fiber interfaces for silicon-on-insulator photonic integrated circuits," *IEEE J. Sel. Top. Quantum. Electron.*, vol. 17, no. 3, pp. 571–580, May/Jun. 2011.

[20] T. Pinguet, B. Analui, E. Balmater, D. Guckenberger, M. Harrison, R. Koumans, D. Kucharski, Y. Liang, G. Masini, A. Mekis, S. Mirsaidi, A. Narasimha, M. Peterson, D. Rines, V. Sadagopan, S. Sahni, T. J. Sleboda, D. Song, Y. Wang, B. Welch, J. Witzens, J. Yao, S. Abdalla, S. Gloeckner, P. De Dobbelaere, and G. Capellini, "Monolithically integrated high-speed CMOS photonic transceivers," in *Proc. 5th IEEE Int. Conf. Group IV Photon.*, Sep. 2008, pp. 362–364.

[21] A. Mekis, S. Gloeckner, G. Masini, A. Narasimha, T. Pinguet, S. Sahni, and P. De Dobbelaere, "A grating-coupler-enabled CMOS photonics platform," *IEEE J. Sel. Top. Quantum. Electron.*, vol. 17, no. 3, pp. 597–608, May/Jun. 2011.

[22] A. Mekis, S. Abdalla, P. M. De Dobbelaere, D. Foltz, S. Gloeckner, S. Hovey, S. Jackson, Y. Liang, M. Mack, G. Masini, R. Novais, M. Peterson, T. Pinguet, S. Sahni, J. Schramm, M. Sharp, D. Song, B. P. Welch, K. Yokoyama, and S. Yu, "Scaling CMOS photonics transceivers beyond 100 Gb/s," in *Proc. SPIE*, 2012, vol. 82650, pp. 82650A-1–82650A-8.

[23] L. Chen, K. Preston, S. Manipatruni, and M. Lipson, "Integrated GHz silicon photonic interconnect with micrometer-scale modulators and detectors," *Opt. Exp.*, vol. 17, no. 17, pp. 15 248–15 256, Aug. 2009.

[24] G. Kim, J. W. Park, I. G. Kim, S. Kim, S. Kim, J. M. Lee, G. S. Park, J. Joo, K. Jang, J. H. Oh, S. A. Kim, J. H. Kim, J. Y. Lee, J. M. Park, D. Kim, D. Jeong, M. Hwang, J. Kim, K. Park, H. Chi, H. Kim, D. Kim, and M. H. Cho, "Low-voltage

high-performance silicon photonic devices and photonic integrated circuits operating up to 30 Gb/s," *Opt. Exp.*, vol. 19, no. 27, pp. 26936–26947, Dec. 2011.
[25] L. Tsung-Yang, A. Kah-Wee, F. Qing, J. Song, X. Yong-Zhong, Y. Ming-Bin, L. Guo-Qiang, and K. Dim-Lee, "Silicon modulators and germanium photodetectors on SOI: Monolithic integration, compatibility, and performance optimization," *IEEE J. Sel. Top. Quantum. Electron.*, vol. 16, no. 1, pp. 307–315, Jan./Feb. 2010.
[26] Z. Zhang, Z. Zhang, B. Huang, C. Cheng, and H. Chen, "CMOS-compatible vertical grating coupler with quasi Mach–Zehnder characteristics," *IEEE Photon. Technol. Lett.*, vol. 25, no. 3, pp. 224–227, Feb. 2013.
[27] D. J. Thomson, Y. Hu, G. T. Reed, and J. M. Fedeli, "Low loss MMI couplers for high performance MZI modulators," *IEEE Photon. Technol. Lett.*, vol. 22, no. 20, pp. 1485–1487, Oct. 2010.
[28] J. Liu, D. D. Cannon, K. Wada, Y. Ishikawa, S. Jongthammanurak, D. T. Danielson, J. Michel, and L. C. Kimerling, "Tensile strained Ge p-i-n photodetectors on Si platform for C and L band telecommunications," *Appl. Phys. Lett.*, vol. 87, no. 1, pp. 11110-1–11110-3, Jul. 2005.
[29] Y. Ishikawa and K. Wada, "Near-infrared Ge photodiodes for Si photonics: Operation frequency and an approach for the future," *IEEE Photon. J.*, vol. 2, no. 3, pp. 306–320, Jun. 2010.
[30] J. Wang, W. Y. Loh, K. T. Chua, H. Zang, Y. Z. Xiong, S. M. F. Tan, M. B. Yu, S. J. Lee, G. Q. Lo, and D. L. Kwong, "Low-voltage high-speed (18 GHz/1 V) evanescent-coupled thin-film-Ge lateral PIN photodetectors integrated on Si waveguide," *IEEE Photon. Technol. Lett.*, vol. 20, no. 17, pp. 1485–1487, Sep. 2008.